Front. Phys.
https://doi.org/10.15302/frontphys.2027.054201
CN 11-5994/O4
ISSN 2095-0462

RESEARCH ARTICLE

Alleviating the responsivity-dark current trade-off in AlGaN solar-blind photodetector via barrier engineering for motion perception

Lihan Li†, Xingyue Wang†, Guanling Yi, Chao Wang, Shuti Li*, Fangliang Gao*

Guangdong Engineering Research Centre of Optoelectronic Functional Materials and Devices, School of Electronic Science and Engineering (School of Microelectronics), South China Normal University, Guangzhou 510631, China

†These authors contributed equally to this work.

*Corresponding authors. E-mail: lishuti@scnu.edu.cn, gaofl@m.scnu.edu.cn

Received September 23, 2026; accepted November 24, 2026

Abstract

Solar-blind photodetectors (SBPDs) are promising for missile trajectory tracking, secure communication, and flame detection, but achieving high responsivity while maintaining low dark current remains a major challenge. Here, we demonstrate an AlGaN-based SBPD that addresses this trade-off through barrier engineering. Incorporating a 20-nm-thick AlGaN barrier layer effectively suppresses dark current while enabling efficient carrier transport via Fowler–Nordheim tunneling under applied bias. The resulting device achieves a high responsivity of 216.4 A W^{-1}, a low dark current of 3.13×10^{-11} A, a specific detectivity of 1.57×10^{15} Jones, a response time of 15.3 ms, and a solar-blind rejection ratio of 7.6×10^{5}. To demonstrate its practical potential, the device is integrated into a motion perception system designed to simulate missile exhaust plume detection. By encoding plume radiation information into 254-nm ultraviolet pulse signals and incorporating realistic background radiation, the system reproduces complex sensing conditions and achieves a recognition accuracy of 95.9% under 40% noise interference. These results establish barrier engineering as an effective approach to balancing responsivity and dark current in AlGaN SBPDs, offering a promising route toward high-performance solar-blind detection and motion perception.

Keywords solar-blind photodetectors, AlGaN, barrier engineering, motion perception

© Higher Education Press 2026

Just Accepted

This is a “Just Accepted” manuscript, which has been examined by the peer-review process and has been accepted for publication. A “Just Accepted” manuscript is published online shortly after its acceptance, which is prior to technical editing and formatting and author proofing. Higher Education Press (HEP) provides “Just Accepted” as an optional and free service which allows authors to make their results available to the research community as soon as possible after acceptance. After a manuscript has been technically edited and formatted, it will be removed from the

"Just Accepted" Web site and published as an Online First article. Please note that technical editing may introduce minor changes to the manuscript text and/or graphics which may affect the content, and all legal disclaimers that apply to the journal pertain. In no event shall HEP be held responsible for errors or consequences arising from the use of any information contained in these "Just Accepted" manuscripts. To cite this manuscript please use its Digital Object Identifier (DOI®), which is identical for all formats of publication.

Alleviating the responsivity-dark current trade-off in AlGaN solar-blind photodetector via barrier engineering for motion perception

Lihan Li†, Xingyue Wang†, Guanling Yi, Chao Wang, Shuti Li*, Fangliang Gao*

[a]Guangdong Engineering Research Centre of Optoelectronic Functional Materials and Devices, School of Electronic Science and Engineering (School of Microelectronics), South China Normal University, Guangzhou 510631, China

†These authors contributed equally to this work.

*Corresponding authors. E-mail: lishuti@scnu.edu.cn, gaofl@m.scnu.edu.cn

Received September 23, 2026; accepted November 24, 2026

Abstract

Solar-blind photodetectors (SBPDs) are promising for missile trajectory tracking, secure communication, and flame detection, but achieving high responsivity while maintaining low dark current remains a major challenge. Here, we demonstrate an AlGaN-based SBPD that addresses this trade-off through barrier engineering. Incorporating a 20-nm-thick AlGaN barrier layer effectively suppresses dark current while enabling efficient carrier transport via Fowler–Nordheim tunneling under applied bias. The resulting device achieves a high responsivity of 216.4 A W^{-1}, a low dark current of 3.13×10^{-11} A, a specific detectivity of 1.57×10^{15} Jones, a response time of 15.3 ms, and a solar-blind rejection ratio of 7.6×10^5. To demonstrate its practical potential, the device is integrated into a motion perception system designed to simulate missile exhaust plume detection. By encoding plume radiation information into 254-nm ultraviolet pulse signals and incorporating realistic background radiation, the system reproduces complex sensing conditions and achieves a recognition accuracy of 95.9% under 40% noise interference. These results establish barrier engineering as an effective approach to balancing responsivity and dark current in AlGaN SBPDs, offering a promising route toward high-performance solar-blind detection and motion perception.

Keywords solar-blind photodetectors, AlGaN, barrier engineering, motion perception

1 Introduction

Solar-blind photodetectors (SBPDs) have attracted considerable attention for military and civilian applications, including secure communications, missile guidance, flame detection, and corona discharge monitoring[1,2]. Wide-bandgap semiconductors, such as SiC, Ga_2O_3, and AlGaN, are widely used in SBPDs because of their excellent spectral selectivity and radiation resistance. For example, Deng et al. developed a $CuNiO_2$/SiC photodetector with a low-light detection limit of 4.6 nW mm^{-2}, a response time of 45 ns, a responsivity of 104.2 mA W^{-1}, and a specific detectivity of 3.4×10^{12} Jones[3]. Similarly, Luo et al. improved the performance of a Ga_2O_3-based SBPD through a thermal pulse treatment, achieving a maximum responsivity of 312.6 A W^{-1} and a short decay time of 40 μs[4]. These advances highlight the potential of wide-bandgap semiconductors for high-performance solar-blind detection.

Among wide-bandgap (WBG) semiconductors, AlGaN has progressed from fundamental research to practical applications owing to its direct and tunable bandgap[5,6]. Building on the well-established AlGaN/GaN high-electron-mobility transistor (HEMT) technology, high-performance photodetectors (PDs) have been developed by exploiting the high carrier mobility of the two-dimensional electron gas (2DEG) formed at the heterointerface. Despite enabling high responsivity, the highly conductive 2DEG channel can also introduce substantial dark current, reducing the photo-to-dark current ratio and ultraviolet (UV)-to-visible rejection ratio[7]. To address these limitations, interrupting the 2DEG conduction channel has proven effective in suppressing dark current while maintaining ultrahigh responsivity[8,9]. However, such performance often requires high operating voltages[10] and complex fabrication processes. Moreover,

growing high-quality Al-rich AlGaN on GaN remains challenging[11], while lattice-mismatch-induced interface defects can further compromise device performance[12]. These limitations have motivated interest in AlGaN-based metal–semiconductor–metal (MSM) solar-blind photodetectors (SBPDs), which consist of two back-to-back Schottky contacts and offer a simple device architecture, straightforward fabrication, fast response, and compatibility with planar integration[12]. Nevertheless, conventional MSM structures lack an effective means of controlling majority-carrier transport, making it difficult to simultaneously achieve high responsivity and low dark current.

Although AlGaN-based MSM photodetectors offer a relatively simple planar architecture, their performance hinges on an inherent trade-off between suppressing dark current and maintaining a strong photoresponse, and recent work has begun to address this challenge through targeted structural design. Studies on solar-blind ultraviolet detection have explored a range of structural strategies: in self-powered devices, band engineering has been employed to suppress dark-current transport[13], while crystal-orientation engineering and optoelectronic-synapse architectures have enabled polarization-sensitive and multifunctional detection, including demonstrations of motion perception[14,15]. These approaches, developed primarily in β-Ga_2O_3-based systems, demonstrate the broader potential of device-structure engineering, even though they involve materials and functions distinct from the AlGaN system examined here.

Closer to the present material system, Dai et al. reported a solar-blind AlGaN MSM photodetector based on an $Al_{0.55}Ga_{0.45}N/Al_{0.4}Ga_{0.6}N/Al_{0.65}Ga_{0.35}N$ heterostructure[16], which establishes a relevant precedent for using AlGaN heterostructure design to regulate carrier distribution and photoresponse in MSM solar-blind photodetectors. A further, more targeted precedent within III-nitride MSM photodetectors was reported by Chuah et al., who introduced a thin $Al_{0.5}Ga_{0.5}N$ surface layer into a GaN MSM photodiode and achieved a higher effective Schottky barrier height along with reduced dark-current leakage[17]. This result supports the underlying rationale that an AlGaN surface layer can modify carrier injection in a nitride MSM structure.

Against this background, we investigate an AlGaN MSM photodetector in which a 20-nm $Al_{0.5}Ga_{0.5}N$ barrier layer is incorporated on an $Al_{0.4}Ga_{0.6}N$ photoactive layer. The barrier is engineered to modify carrier injection at the metal/semiconductor contacts, suppressing dark-current injection while permitting field-assisted carrier transport under an applied bias. The present work aims to clarify how barrier engineering affects the dark current–photoresponse trade-off in this device architecture. To evaluate this relationship, we examine the measured dark and illuminated I–V characteristics, transient response, and power-dependent photoresponse, and further demonstrate the device within a motion-perception system. The resulting AlGaN SBPD achieves a high responsivity of 216.4 $A \cdot W^{-1}$, a low dark current of 3.13×10^{-11} A, a specific detectivity of 1.57×10^{15} Jones, a fast response time ($\tau_r \approx 15.3$ ms), and a high rejection ratio ($R_{254}/R_{365} \approx 7.6\times10^5$). Moreover, the high-performance AlGaN SBPD is integrated into a motion-perception system, where it retains 95.9% recognition accuracy even at a noise level as high as 40%, illustrating its potential for practical deployment. These results indicate that the proposed AlGaN SBPD offers a promising route toward stable and efficient solar-blind sensing systems.

2 Materials and Methods

2.1 Material Epitaxy

The growth process was carried out using the MOCVD technique on a 2-inch *c*-plane sapphire substrate. TMAl, TMGa, and NH_3 were employed as the precursors for Al, Ga, and N, respectively. Initially, a 2-μm-thick AlN buffer layer was grown, followed by a ~300 nm $Al_{0.6}Ga_{0.4}N/Al_{0.4}Ga_{0.6}N$ intermediate layer. Finally, a 300-nm-thick $Al_{0.4}Ga_{0.6}N$

photoactive epilayer and a 20-nm-thick $Al_{0.5}Ga_{0.5}N$ barrier layer were deposited sequentially. Through tuning the Al/Ga source ratio, the designed Al content of each layer can be realized.

2.2 Device Fabrication

The photodetector was fabricated by using a simple non-etching planar process. Prior to device fabrication, the wafer sample was individually cleaned with acetone, isopropanol (IPA), and deionized (DI) water for 5 min and immersed in a NH_4OH:H_2O_2: DI water (1:1:3) solution for 5 min to remove particulate contaminants. Then, the electrode pattern was formed by standard photolithography. Next, Ni/Au (20 nm/50 nm) interdigital electrodes were directly deposited on the clean wafer surface by thermal evaporation.

2.3 Characterization

The morphology of the photodetector was observed using an optical microscope (PSAIC-B200). The material characterization was carried out using high-resolution X-ray diffraction (HR-XRD) to evaluate the structural and crystal quality of the grown photoactive epilayer. Additionally, atomic force microscopy (AFM) was employed to assess the surface roughness of the film. All electrical properties were measured in air using a four-probe station equipped with a semiconductor device analyzer (Keithley 2636 B).

2.4 Optoelectronic characterization.

The photocurrent and photoresponse were measured under illumination from a 254-nm LED (CZERSHISI, CZ-005). The optical power at the device plane was recorded with a calibrated optical power meter (Shenzhen Linshang Technology Co., Ltd., LS125) fitted with a detector (UVA-X1) appropriate for the measurement wavelength. The illuminated spot at the sample plane covered the entire active region and had an area of 0.2826 cm^2; for the interdigitated-electrode device, the effective illuminated area was defined as the spot area minus the portion shadowed by the metal electrodes, yielding a value of 0.000528 cm^2. All measurements were performed at room temperature (26 °C), with the bias voltage swept from −6 V to 6 V unless otherwise specified.

3 Results and Discussion

Fig. 1(a) shows a photograph of the fabricated photodetector arrays grown on a 2-inch sapphire substrate; each 1 × 1 cm^2 array contains 10 × 10 devices, and a single photodetector serves as the proof-of-concept device, whose epitaxial structure is illustrated in Fig. 1(b) and revealed by scanning electron microscopy (SEM) in Fig. 1(c). Fig. 1(d) displays the symmetric high-resolution X-ray diffraction (HR-XRD) peaks of $Al_{0.4}Ga_{0.6}N$ (0002), $Al_{0.5}Ga_{0.5}N$ (0002), $Al_{0.6}Ga_{0.4}N$ (0002), and AlN (0002), located at 35.18°, 35.28°, 35.43°, and 36.03°, respectively. The recorded full width at half maximum (FWHM) of the $Al_{0.4}Ga_{0.6}N$ peak is approximately 0.05°, indicating superior crystal quality of the $Al_{0.4}Ga_{0.6}N$ film, which is primarily attributed to the effective alleviation of lattice mismatch by the $Al_{0.6}Ga_{0.4}N$/$Al_{0.4}Ga_{0.6}N$ intermediate layer. The surface morphology of the heteroepitaxial AlGaN epilayer was further examined by atomic force microscopy (AFM); as shown in the 2 × 2 μm^2 AFM image in Fig. 1(e), the root-mean-square surface roughness is approximately 813 pm, indicating a smooth surface and uniform growth. The optical properties of the wafer samples were characterized by photoluminescence (PL) spectroscopy. As shown in Fig. 1(f), the emission peak centered at 277.2 nm is assigned to the $Al_{0.4}Ga_{0.6}N$ channel, whereas the shorter-wavelength shoulder at 268.9 nm originates from the $Al_{0.5}Ga_{0.5}N$ barrier.

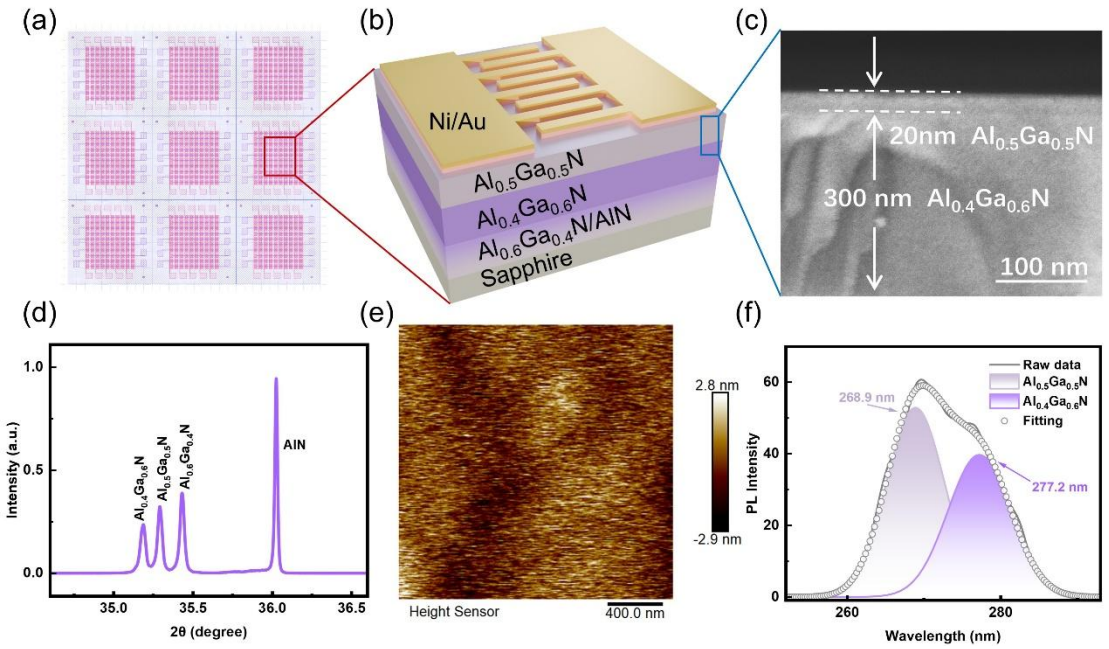


Fig. 1 (a) A photograph of fabricated wafer-scale device arrays on a 2-inch sapphire substrate. (b) Schematic of the device structure. (c) Cross-sectional SEM image of $Al_{0.5}Ga_{0.5}N/Al_{0.4}Ga_{0.6}N$ material stack. (d) General HR-XRD scan of the grown sample. (e) AFM image of the AlGaN epilayer. (f) Room-temperature PL spectrum measured using a 233-nm laser as the excitation source.

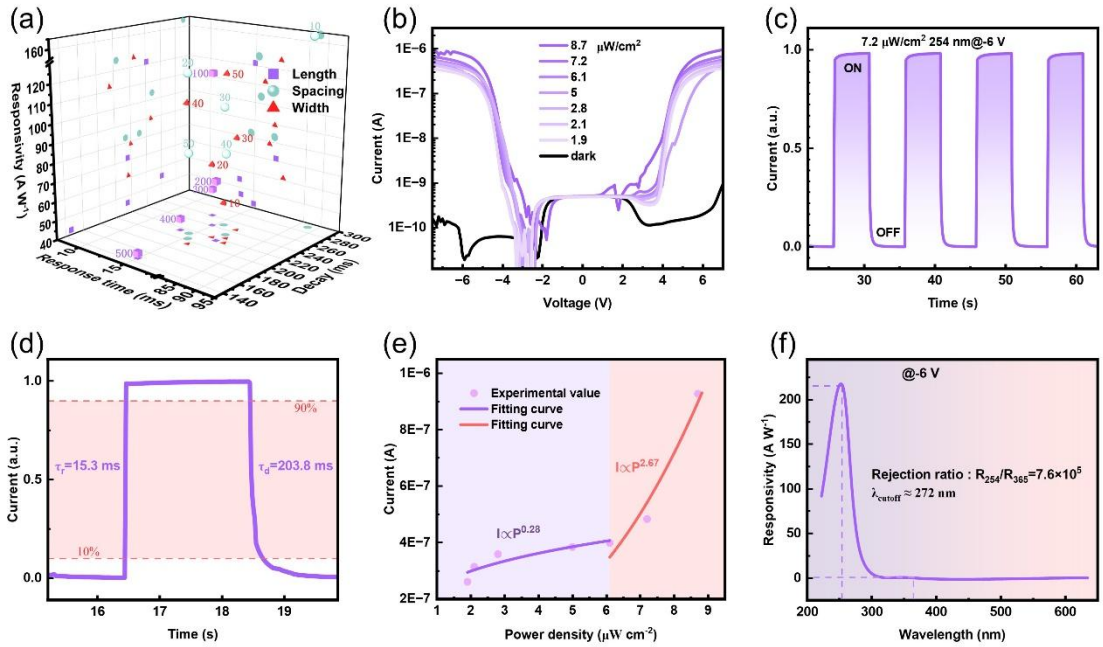


Fig. 2 (a) The responsivity, response time, and decay time of devices with different geometry of interdigital electrode. (b) The I–V curve of the device under dark and 254 nm illumination with increasing power densities. (c) Time-dependent photoresponse of the device at −6 V bias with 7.2 μW cm^{-2} 254 nm illumination. (d) Response speed of the detector under 254 nm illumination at 7.2 μW/cm² (e) I_{ph} dependence as a function of various optical powers at 254 nm. (f) Spectral response of the photodetector at −6 V bias.

As shown in Fig. 1(b), the fabricated photodetector employs Ni/Au Schottky contacts. The geometry of the interdigital electrodes, including the length (l), width (w), and spacing (s), was optimized to improve the photocurrent collection efficiency of the AlGaN photodetectors (Fig. S1–S4). By comprehensively evaluating the responsivity, response time, and decay time of devices with different electrode geometries (Fig. 2(a)), the optimal parameters were determined to be l = 300 μm, w = 50 μm, and s = 20 μm, and the device with these optimized electrodes exhibits enhanced responsivity and a fast response time. Fig. 2(b) plots the I–V characteristics of the photodetector under dark conditions and under 254-nm UV LED illumination at optical power densities ranging from 1.9 to 8.7 μW cm^{-2}. At low bias, the dark and illuminated I–V curves nearly overlap, reflecting a small photocurrent increment in this bias range; this behavior is consistent with the limited carrier injection and collection imposed by the weak electric field across the back-to-back Schottky contacts. As the applied bias magnitude increases, the current rises rapidly above approximately $|V_{ds}| > 4.2$ V, and the photocurrent reaches saturation at −6 V. This high-bias current increase indicates that a field-assisted transport process becomes dominant, and the underlying physical mechanism is discussed later. Fig. 2(c) shows the time-dependent response current of the photodetector to periodically switched DUV light at a bias of −6 V, presenting a repeatable and stable response with an on/off period of 2 s. Stability is a critical performance factor governing the practical utility of AlGaN solar-blind photodetectors, and the long-term continuous I–t curve was therefore measured under 254-nm illumination and −6 V bias (Fig. S5). After 1200 s of continuous illumination over 300 cycles, no significant decrease in photocurrent was observed, demonstrating that the AlGaN photodetector offers excellent operational stability and is a reliable candidate for practical applications. Fig. 2(d) presents the normalized current–time trace of a single response cycle; the time required for the photocurrent to rise from 10% to 90% and to decay from 90% to 10% defines the rise time (τ_r = 15.3 ms) and decay time (τ_d = 203.8 ms) of the AlGaN SBPD, respectively. The relatively slow decay may be associated with the delayed release and recombination of carriers trapped at defect or interface states, which can sustain the photocurrent after illumination, while polarization-induced band bending may also influence carrier separation and extraction in the AlGaN heterostructure; however, the present measurements do not directly identify the origin of this slow decay.

Responsivity (R), detectivity (D^*), external quantum efficiency (EQE), sensitivity (S), and linear dynamic range (LDR) are the principal figures of merit for SBPDs, and their specific definitions are given in Note. S1. R was calculated to be 216.4 A W^{-1}, a value far exceeding the 100% quantum-efficiency limit, which indicates the presence of an internal gain mechanism in the device. To investigate this gain mechanism further, power-dependent photoresponse measurements were performed at a fixed bias of −6 V over optical power densities from 1.9 to 8.7 μW cm^{-2}. The power index α was obtained by fitting the relation $I_{ph} \propto P^{\alpha}$ [18]. As shown in Fig. 2(e), α = 0.28 was extracted from the linear fit of the measured I_{light} for power densities below 6.1 μW cm^{-2}, whereas α = 2.67 was obtained above 6.1 μW cm^{-2}. In conventional photodetectors, $\alpha < 1$ indicates photogeneration and trapping of carriers [19], while $\alpha > 1$ suggests a photocurrent gain mechanism [7]. These observations provide a possible framework for interpreting the two power-dependent regimes, and the corresponding carrier-transport picture is discussed together with the band-diagram schematic in Fig. 4(c). Finally, the spectral response of the SBPD was characterized. As shown in Fig. 2(f), the rejection ratio R_{254}/R_{365} reaches approximately 7.6×10^5, and the cutoff wavelength (λ_{cutoff}) is identified at approximately 272 nm, defined by the 1/e point of the R peak, revealing excellent spectral selectivity within the solar-blind region.

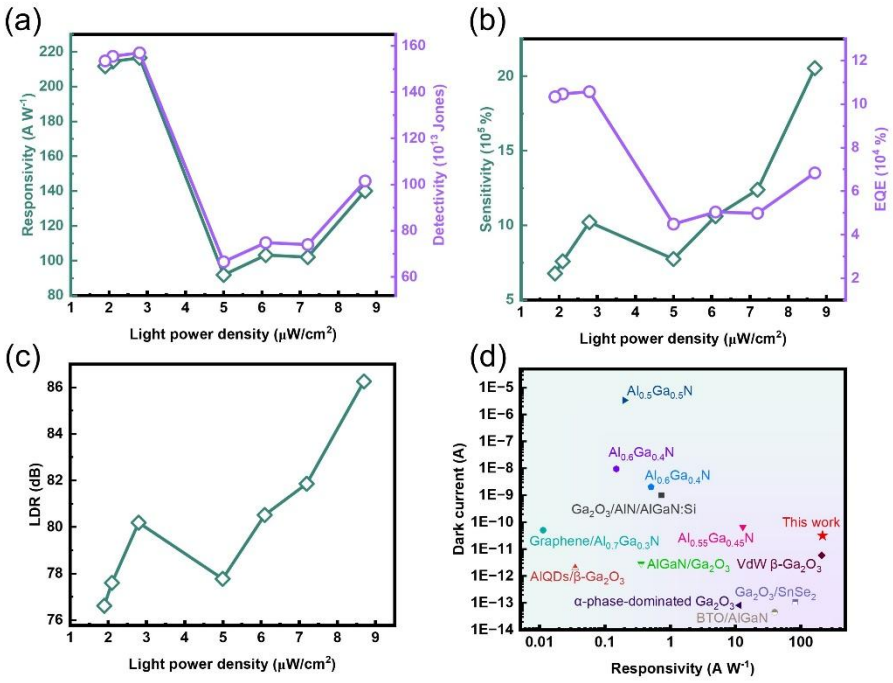


Fig. 3 (a) R and D*, (b) S and EQE, (c) LDR of the AlGaN photodetector under different 254 nm light intensity. (d) Summary of R and dark current of various photodetectors.

Fig. 3(a)-(c) summarize the key photodetection parameters of the AlGaN SBPDs measured under various optical power densities at a bias of −6 V. As shown in Fig. 3(a), maximum R and D^* values of 216.4 A W^{-1} and 1.57×10^{15} Jones are achieved at an optical power density of 2.8 μW cm^{-2}, respectively. Notably, the decline and rise of R with increasing optical power correspond to the $\alpha = 0.28$ and $\alpha = 2.67$ regimes in Fig. 2(e), respectively; since $R = I_{ph}/P$ and the power-law relation $I_{ph} \propto P^{\alpha}$ yields $R \propto P^{\alpha-1}$, the two trends follow directly from this dependence. At low optical power, this behavior is attributed to carrier trapping by defects and trap states, which leads to $\alpha < 1$; at high optical power, the trap states are gradually filled, and photogenerated carriers screen the polarization field, which may restore the 2DEG channel and give rise to additional photoconductive gain. The device reaches an S as high as 2.05×10^{6}% and an LDR of 86.2 dB, indicating a relatively large I_{light}/I_{dark} ratio, while its EQE reaches a remarkable 1.05×10^{5}%. Owing to its high R and low I_{dark}, the AlGaN SBPD outperforms recent SBPDs based on AlGaN, Ga_2O_3, and their heterostructures[20–33], as illustrated in Fig. 3(d).

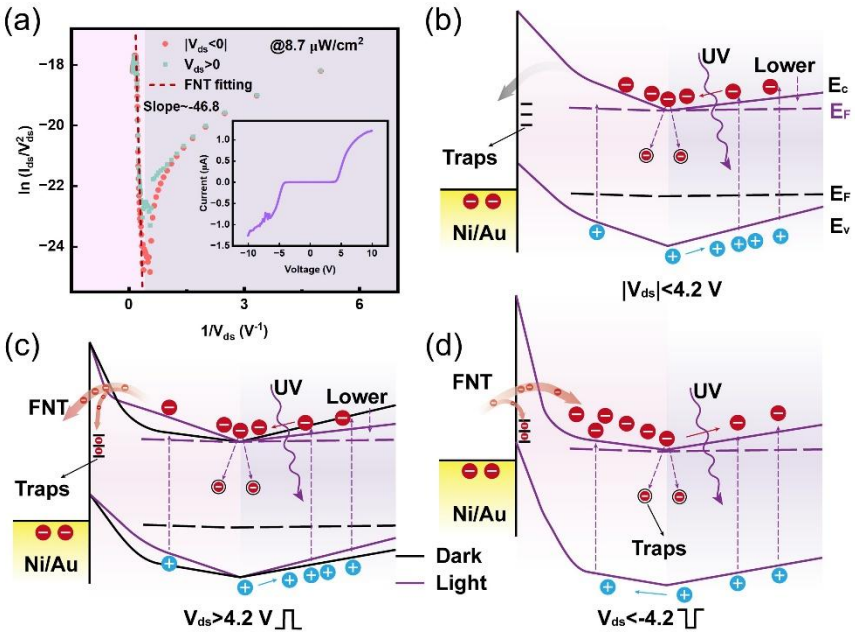


Fig. 4 (a) The Fowler-Nordheim plot of $\ln(I_{ds}/V_{ds}^2)$ versus $1/V_{ds}$. Schematic of the band diagrams to reveal tunning mechanism under(b) low bias, $|V_{ds}| < 4.2V$; (c) high positive bias, $V_{ds} > 4.2V$; and (d) high negative bias, $V_{ds} < -4.2V$. The black lines represent the valence-band edge, conduction-band edge, and Fermi level under dark conditions, whereas the purple lines represent those under illumination. The triangular barrier is primarily located at the interface between the $Al_{0.5}Ga_{0.5}N$ layer and the metal electrode. The diagrams indicate the proposed roles of interfacial trap states, photogenerated carriers, and field-induced barrier modulation.

The significantly improved photoresponse can be attributed to tunneling mechanism enhanced by barrier engineering. The specific tunneling mechanism was further determined by replotting the I-V curve in Fig. 4(a) with the Simmons approximation, where direct tunneling (DT) was obtained at low V_{ds} and FNT appeared at high V_{ds}[34]. The DT and FNT can be expressed as follows[1]:

$$I_{DT} \propto Vexp\left(-\frac{4\pi\sqrt{2m^*\varphi}}{h}\right), \quad (1)$$

$$I_{FNT} \propto V^2exp\left(-\frac{8\pi d\sqrt{2m^*\varphi}}{3heV}\right), \quad (2)$$

where d, m^*, φ, and h denote the tunneling thickness, effective electron mass, tunneling barrier height, and Planck constant, respectively[1]. Accordingly, a plot of $\ln(I_{ds}/V_{ds}^2)$ versus $1/V_{ds}$ should exhibit a linear negative slope for FNT, whereas DT emerges when the slope increases exponentially[35]. To further examine the temperature-dependent electrical properties of the device under negative bias, temperature-dependent I–V measurements were carried out from 180 to 380 K, with the results presented in Fig. S7 (Supporting Information). Within the device operating range of 0 to $-6V$, the current in the high-field region between approximately $-4.2$and $-6V$ shows a comparatively weak temperature dependence, consistent with a field-assisted tunneling contribution. As shown in Fig. 4(a), FNT occurs under both large positive and large negative voltages, and the threshold voltage (V_{th}) for FNT was approximately extracted to 2.38 V (1/0.42) that corresponds to φ/e, indicating that the tunneling barrier is about 2.38 eV. To better understand the tunneling mechanism underlying the high photodetection performance, we examined the energy band alignment and carrier distribution, as shown in Fig. 4(b)-(d). At low voltages (Fig. 4(b)), the barrier changes insignificantly, so that almost no charge flows and the measured current remains extremely low. At a large forward

bias (V_{ds} > 4.2 V), a triangular potential barrier forms at the interface, as shown in Fig. 4(c), allowing electrons to cross the barrier via FNT. At a large negative bias (V_{ds} < −4.2 V), the energy bands bend sharply under the applied electric field, as illustrated in Fig. 4(d), and the tunneling barrier is modulated into a triangular shape, which likewise leads to FNT current.

Building on the tunneling analysis above, we further elaborate the gain mechanism with reference to the band diagram in Fig. 4(c). Carrier traps distributed within the bandgap and at the metal–semiconductor interface act as recombination centers under illumination, which accounts for the weak light-intensity dependence of the photocurrent (α < 1)[36–39]. The photocurrent gain under high optical power may arise from trap saturation together with the reduction of the built-in field and barrier height caused by the large population of photogenerated carriers. Under DUV illumination at higher optical power, the carrier concentration rises nonlinearly and fills all available defect states; the defects can then no longer capture additional carriers and cease to govern the light-intensity dependence of the device. Meanwhile, the photogenerated electron–hole pairs in AlGaN are separated by the polarization-induced field, which weakens the built-in field and raises the Fermi level above E_c, thereby recovering and widening the 2DEG channel and contributing to photoconductive gain[40]. On the other hand, the accumulation of photogenerated holes lowers the barrier height, facilitating electron escape and transport[7], which may constitute another possible mechanism for the observed high gain.

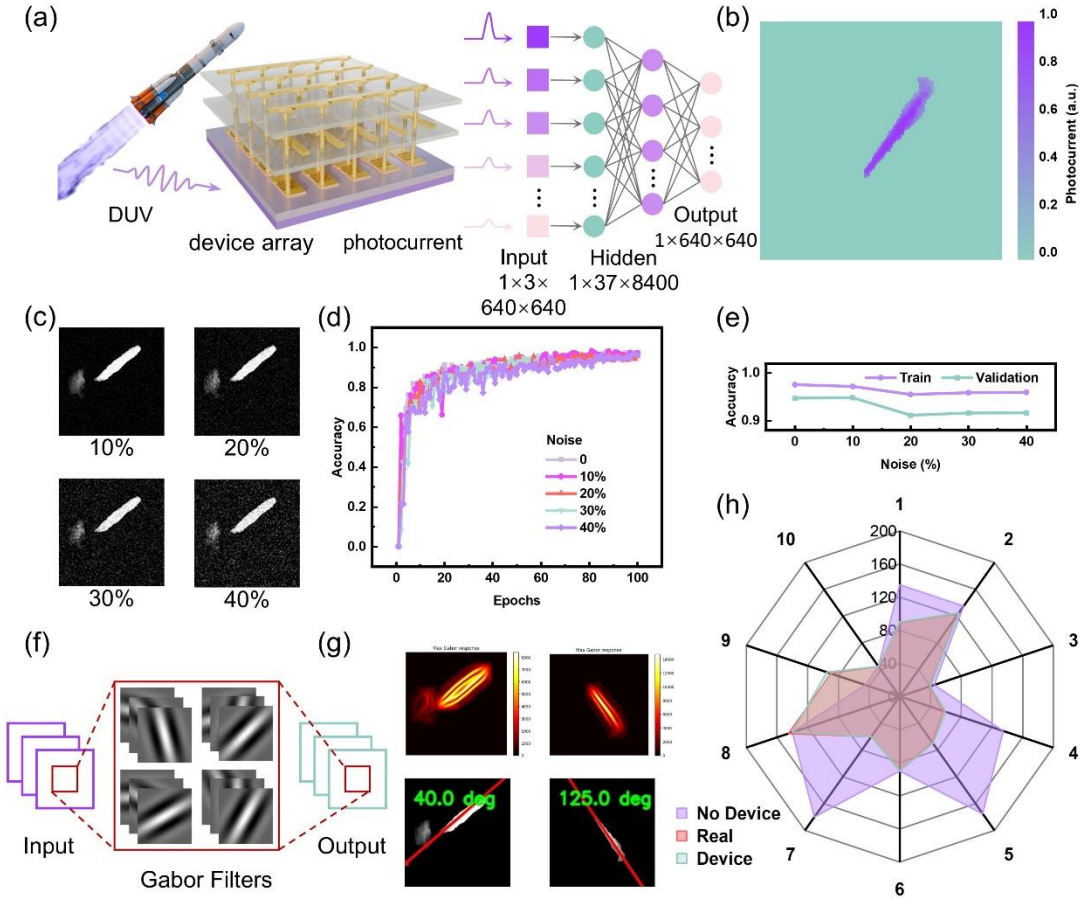


Fig. 5 A motion perception system based on the AlGaN SBPD. (a) Illustration of the experimental progress for motion perception. (b) The readout current maps of tail flame. (c) Motion images under three different noise levels. (d) Train accuracy versus running epochs. (e) Recognition accuracy after 100 training epochs of tail flame versus the

noise levels. (f) Modulation process of the Gabor filters. (g) Direction discrimination of tail flame using the Gabor filters based on AlGaN SBPD-processed signals. (h) Real angles and recognition angles of 10 tail flame examples under unenhanced and preprocessed image scenes.

Beyond device-level photodetection, the integration of solar-blind UV sensing with intelligent signal processing has also been explored. For example, α-In_2Se_3-based phototransistors have been used for solar-blind UV detection and optoelectronic neuromorphic computing, including noise-tolerant image recognition[41], offering a related example of combining UV sensing with information processing. In modern defense systems, real-time perception of missile motion is a prerequisite for early warning and interception; during missile launch, intense short-wavelength UV radiation, concentrated particularly in the solar-blind spectral region, is generated in the exhaust plume and its surrounding environment[42]. The present AlGaN SBPD exhibits intrinsic sensitivity to this DUV radiation, making it well suited to missile motion perception. To demonstrate its practical potential, the high-performance AlGaN SBPD was integrated into a motion-perception system, as shown in Fig. 5(a). The system first extracts the exhaust plume region from the input image and maps its intensity distribution into 254-nm ultraviolet pulse signals of varying amplitudes; meanwhile, the non-plume regions are converted into background illumination, forming a composite radiation field of target and background radiation. This approach realistically simulates plume-target detection under complex background conditions, so that the generated device response more closely represents the sensing signals encountered in real-world scenarios, and Fig. 5(b) depicts the corresponding tail-flame readout current maps.

The robustness of the motion-perception system is critical to the performance of such a sensing application. To evaluate this robustness, Gaussian noise at different levels was introduced into the images to simulate non-ideal realistic conditions, as shown in Fig. 5(c); notably, the recognition accuracy still reaches 95.9% even at a noise level as high as 40% (Fig. 5(d)), and after 100 training epochs the tail-flame recognition accuracy is very close to the ideal value (Fig. 5(e)). These results indicate that the system successfully extracts motion features from realistic sensing signals with favorable robustness. In practical scenarios, the motion trajectory of the tail flame provides vital operational data, enabling precise determination of aircraft orientation and flight phase. Accordingly, Gabor filters were employed to extract the directional information of the tail flame, effectively capturing relevant features along different orientations, as shown in Fig. 5(f); the convolution results and the corresponding directions, referenced to the positive x-axis, are given in Fig. 5(g). Fig. 5(h) shows that the angle discrimination results after preprocessing by the AlGaN SBPD are much closer to the true angles, with accuracy rising significantly from 65.6% to 98% across the 10 test cases. These results further demonstrate the motion-perception capability of the device. In summary, the motion-perception system based on the proposed AlGaN SBPD shows promise for high-precision tail-flame sensing tasks.

4 Conclusions

In summary, an AlGaN SBPD based on barrier engineering was fabricated to alleviate the trade-off between high responsivity and low dark current in AlGaN-based solar-blind detectors. The device achieves a high R of 216.4 $A \cdot W^{-1}$, a D^* of 1.57×10^{15} Jones, a low I_{dark} of 3.13×10^{-11} A, and a fast rise time τ_r of 15.3 ms, confirming its suitability for solar-blind sensing. This excellent optoelectronic performance arises from the barrier-induced suppression of dark current combined with the field-enhanced FNT transport under applied bias. Furthermore, the motion-perception system built on this AlGaN SBPD achieves a real-time missile trajectory recognition accuracy of 95.9% even under a 40% noise level, and improves angle-discrimination accuracy from 65.6% to 98% across the 10 test cases. This work

is expected to facilitate the practical deployment of WBG devices, particularly in solar-blind detection-related applications.

Declarations The authors declare that there are no financial interests.

Acknowledgements This work was supported by Advanced Materials-National Science and Technology Major Project (Grant No. 2026ZD0622700), the National Natural Science Foundation of China (Grant Nos. 62375090, 52002135 and 62374062), Guangdong Basic and Applied Basic Research Foundation (Grant Nos. 2024A1515140064, 2023B1515120071, 2023A0505050131, 2022A0505050066, and 2024A1515011081), the Characteristic Innovation Project of Universities in Guangdong Province (Grant No. 2023KTSCX028), and the Science and Technology Program of Guangzhou, China (Grant No. 2024A04J6456).

References

1. Li. Z., Yan T., Fang X., "Low-dimensional wide-bandgap semiconductors for UV photodetectors," *Nat. Rev. Mater.* **8**, 587–603 (2023).
2. Xie C., Lu X.-T., Tong X.-W., *et al.*, "Recent progress in solar-blind deep-ultraviolet photodetectors based on inorganic ultrawide bandgap semiconductors," *Adv. Funct. Mater.* **29**, 1806006 (2019).
3. Deng W., Fan X., Du Y., *et al.*, "Ultrasensitive and ultrafast self-powered ultraviolet photodetector array for solar-blind and weak-light imaging," *Adv. Mater.* **38**, e14968 (2025).
4. Luo L., Huang H., Yang L., *et al.*, "Ultra-fast gallium oxide solar-blind photodetector with novel thermal pulse treatment," *Adv. Mater*. **37**, 2414130 (2025).
5. Kneissl M., Seong T.-Y., Han J., *et al.*, "The emergence and prospects of deep-ultraviolet light-emitting diode technologies," *Nat. Photonics.* **13**, 233–244 (2019).
6. Lu J., Lv Z., Jiang H., "AlGaN solar-blind phototransistor capable of directly detecting sub-fW signals: self-depletion and photorecovery of full-channel 2DEG enabled by a quasi-pseudomorphic structure," *Photonics Res.* **11**, 1217 (2023).
7. Zhang Y.-Y., Zheng Y.-X., Lai J.-Y., *et al.*, "High performance flexible visible-blind ultraviolet photodetectors with two-dimensional electron gas based on unconventional release strategy," *ACS Nano*. **15**, 8386–8396 (2021).
8. Zhang H., Liang F., Song K., *et al.*, "Demonstration of AlGaN/GaN-based ultraviolet phototransistor with a record high responsivity over 3.6×10^7 A/W," *Appl. Phys. Lett.* **118**, 242105 (2021).
9. Wang H., You H., Xu Y., *et al.*, "High-responsivity and fast-response ultraviolet phototransistors based on enhanced p-GaN/AlGaN/GaN HEMTs," *ACS Photonics.* **9**, 2040–2045 (2022).
10. Pu Y., Liang Y.C., "100 mV ultra-low bias AlGaN/GaN photodetector based on fin-shaped capacitor configuration for future integrated optoelectronics," *ACS Photonics.* **10**, 1293–1301 (2023).
11. Zhong Y., Berikaa E., Lu J., *et al.*, "Molecular beam epitaxial growth and optical characterization of AlGaN nanowires with reduced substrate temperature," *AIP Adv.* **10**, 25022 (2020).
12. Cai Q., You H., Guo H., *et al.*, "Progress on AlGaN-based solar-blind ultraviolet photodetectors and focal plane arrays," *Light: Sci. Appl.* **10**, 1–31 (2021).
13. Pan J., Li C., Geng H., et al., "Band engineering to suppress dark current in self-powered solar-blind photodetectors for optoelectronics in harsh environments," *Phys. Rev. Applied.* **24**, 064043 (2025).
14. Wang Z., Wu C., Wu F., et al., "Polarization-Modulated Solar-Blind Optoelectronic Synapse Based on Anisotropic β-Ga_2O_3 Crystal for Logic Operations and Motion Perception," *ACS Photonics.* **12**, 5291–5301 (2025).

15. Zhang G., Wang Z., Chen S., et al., "Fabrication of Highly Anisotropic Large-Area β-Ga_2O_3 Thin Films via Crystal Orientation Engineering for Multifunctional Solar-Blind Polarization-Sensitive Photodetectors," *Laser Photonics Rev.* **19**, e00255 (2025).
16. Dai S., Gu Y., Guo J., et al., "Metal-semiconductor-metal solar-blind ultraviolet photodetector based on an$Al_{0.55}Ga_{0.45}N/Al_{0.4}Ga_{0.6}N/Al_{0.65}Ga_{0.35}N$ heterostructures," *Opt. Express*. **31**, 30495–30504 (2023).
17. L. S. Chuah, Z. Hassan, and H. Abu Hassan, Performance improvement of large area GaN MSM photodiode with thin AlGaN surface layer, *Microelectron. Int.* **27**, 140–142 (2010).
18. Chen K., Wang X., Zou C., *et al.*, "Two-In-one: end-emitting blue LED and self-powered UV photodetector based on single trapezoidal PIN GaN microwire for ambient light UV monitoring and feedback," *Small Methods.* **7**, 2300138 (2023).
19. Gong X., Tong M., Xia Y., *et al.*, "High-detectivity polymer photodetectors with spectral response from 300 nm to 1450 nm," *Science*. **325**, 1665–1667 (2009).
20. Wang H., Zhou C., Li P., *et al.*, "High-sensitivity and fast-response solar-blind photodetectors via band offset engineering for motion tracking," *Nat. Commun.* **16**, 8175 (2025).
21. Pandit B., Cho J., "Solar-blind ultraviolet photodetectors with thermally reduced graphene oxide formed on high-Al-content AlGaN layers," *AIP Adv.* **11**, 115322 (2021).
22. Nie Y., Jiao S., Yang S., *et al.*, "Achieving ultra-low dark current in β-Ga_2O_3 photoconductive photodetectors for anti-interference optical human–machine interaction systems via gallium interstitials engineering," *Small*. **21**, 2501442 (2025).
23. Choubey B., Ghosh K., "Highly sensitive and fast response AlGaN-based MSM solar-blind photodetector," *IEEE Trans. Electron. Devices.* **72**, 4204–4210 (2025).
24. Ning J., Yang Z., Wu H., *et al.*, "Van der waals β-Ga_2O_3 thin films on polycrystalline diamond substrates," *Nat. Commun.* **16**, 8144 (2025).
25. Hou X., Sun H., Long S., *et al.*, "Ultrahigh-performance solar-blind photodetector based on α-phase-dominated Ga_2O_3 film with record low dark current of 81 fA," *IEEE Electron. Device. Lett.* **40**, 1483–1486 (2019).
26. Rathkanthiwar S., Kalra A., Solanke S.V., *et al.*, "Gain mechanism and carrier transport in high responsivity AlGaN-based solar blind metal semiconductor metal photodetectors," *J. Appl. Phys.* **121**, 164502 (2017).
27. Xie F., Li Y., Liu Y., *et al.*, "Effect of $C_{44}H_{30}N_4O_4$ surface modification on the performance of $Al_{0.6}Ga_{0.4}N$ MSM photodetectors," *IEEE Trans. Electron. Devices*. **69**, 4337–4341 (2022).
28. Dai S., Gu Y., Guo J., *et al.*, "Metal-semiconductor-metal solar-blind ultraviolet photodetector based on heterostructures," *Opt. Express*. **31**, 30495–30504 (2023).
29. Yoshikawa A., Ushida S., Nagase K., *et al.*, "High-performance solar-blind $Al_{0.6}Ga_{0.4}N/Al_{0.5}Ga_{0.5}N$ MSM type photodetector," *Appl. Phys. Lett.* **111**, 191103 (2017).
30. Huang Z., Zhang Z., Wang Y., *et al.*, "High-performance type-I Sn-doped-$Ga_2O_3/SnSe_2$ heterojunction photodetectors enabled by fowler-nordheim tunneling," *Appl. Phys. Lett.* **127**, 62102 (2025).
31. Qi X., Qian L., Hong X., *et al.*, "Solar-blind UV PD based on the BTO/$Al_xGa_{1-x}N$ heterostructure for imaging and optical communication," *IEEE Trans. Electron. Devices.* **72**, 5054–5059 (2025).
32. Wu H., Pan J., Wu C., *et al.*, "Quantum-confinement-effect-tuned cascade AlQDs/β-Ga_2O_3 heterojunctions for ultrasensitive solar-blind photodetection and interference-resistant imaging," *Small.* **21**,2504173 (2025).
33. He X., Sun R., Xu X., *et al.*, "Excellent wavelength selectivity of p-AlGaN/n-Ga_2O_3 solar-blind UVC PD," *ACS Appl. Mater. Interfaces.* **16**, 64146–64155 (2024).
34. Cong X., Zheng Y., Huang F., *et al.*, "Efficiently band-tailored type-III van der waals heterostructure for tunnel diodes and optoelectronic devices," *Nano Res.* **15**, 8442–8450 (2022).

35. Zhou X., Hu X., Zhou S., *et al.*, "Tunneling diode based on WSe_2/SnS_2 heterostructure incorporating high detectivity and responsivity," *Adv. Mater.* **30**, 1703286 (2018).
36. Liao Z.-M., Hou C., Liu L.-P., et al., "Temperature dependence of photoelectrical properties of single selenium nanowires," Nanoscale Res. Lett. **5**, 926–929 (2010).
37. Zhang X., Jie J., Zhang W., et al., "Photoconductivity of a single small-molecule organic nanowire," Adv. Mater. **20**, 2427, (2008).
38. Mukherjee B., Cai Y., Tan H.R., et al., "NIR schottky photodetectors based on individual single-crystalline GeSe nanosheet," ACS Appl. Mater. Interfaces. **5**, 9594–9604 (2013).
39. Garg M., Tak B.R., Rao V.R., et al., "Giant UV photoresponse of GaN-based photodetectors by surface modification using phenol-functionalized porphyrin organic molecules," ACS Appl. Mater. Interfaces. **11**, 12017–12026 (2019).
40. Peng Z., Wu M., Lv Z., et al., "Effective mitigation of persistent photoconductivity in AlGaN solar-blind field-effect phototransistors via In-situ SiNx passivation," IEEE Electron. Device. Lett. **45**, 2074–2077 (2024).
41. Cai Y., Yang J., Wang F., et al., "Ultrasensitive solar-blind ultraviolet detection and optoelectronic neuromorphic computing using α-In_2Se_3 phototransistors," Front. Phys. **18**, 33308 (2023).
42. Wang Z., Wu C., Wu F., et al., "Polarization-modulated solar-blind optoelectronic synapse based on anisotropic β-Ga2O3 crystal for logic operations and motion perception," ACS Photonics **12**, 5291-5301 (2025).